PAPER

Structurally stable Mg-doped P2-Na$_{2/3}$Mn$_{1-y}$Mg$_y$O$_2$ sodium-ion battery cathodes with high rate performance: insights from electrochemical, NMR and diffraction studies†

Raphaële J. Clément,[a] Juliette Billaud,[b] A. Robert Armstrong,[b] Gurpreet Singh,[c] Teófilo Rojo,[c] Peter G. Bruce[bd] and Clare P. Grey*[a]

Sodium-ion batteries are a more sustainable alternative to the existing lithium-ion technology and could alleviate some of the stress on the global lithium market as a result of the growing electric car and portable electronics industries. Fundamental research focused on understanding the structural and electronic processes occurring on electrochemical cycling is key to devising rechargeable batteries with improved performance. We present an in-depth investigation of the effect of Mg doping on the electrochemical performance and structural stability of Na$_{2/3}$MnO$_2$ with a P2 layer stacking by comparing three compositions: Na$_{2/3}$Mn$_{1-y}$Mg$_y$O$_2$ (y = 0.0, 0.05, 0.1). We show that Mg substitution leads to smoother electrochemistry, with fewer distinct electrochemical processes, improved rate performance and better capacity retention. These observations are attributed to the more gradual structural changes upon charge and discharge, as observed with synchrotron, powder X-ray, and neutron diffraction. Mg doping reduces the number of Mn^{3+} Jahn–Teller centers and delays the high voltage phase transition occurring in P2-Na$_{2/3}$MnO$_2$. The local structure is investigated using ^{23}Na solid-state nuclear magnetic resonance (ssNMR) spectroscopy. The ssNMR data provide direct evidence for fewer oxygen layer shearing events, leading to a stabilized P2 phase, and an enhanced Na-ion mobility up to 3.8 V *vs.* Na$^+$/Na upon Mg doping. The 5% Mg-doped phase exhibits one of the best rate performances reported to date for sodium-ion cathodes with a P2 structure, with a reversible capacity of 106 mA h g^{-1} at the very high discharge rate of 5000 mA g^{-1}. In addition, its structure is highly reversible and stable cycling is obtained between 1.5 and 4.0 V *vs.* Na$^+$/Na, with a capacity of approximately 140 mA h g^{-1} retained after 50 cycles at a rate of 1000 mA g^{-1}.

Broader context

Rechargeable lithium (Li)-ion batteries are currently the technology of choice for applications in portable electronics and in the electric vehicle industry. Yet, Li sources are scarce and discretely located on Earth, driving the search for novel, more sustainable chemistries for electrical energy storage. Sodium(Na)-based systems are one of the more promising emerging technologies, and much effort is currently put into finding high performance Na-ion electrodes and electrolytes. Sodium transition metal oxides (Na$_x$TMO$_2$) stand out as good cathode materials with a high volumetric energy density. Electrodes composed of a combination of low cost, abundant elements, *e.g.* Na, Mg, Fe, Mn, are ideally suited for large-scale applications such as grid storage. Here, we focus on a family of layered P2-Na$_{2/3}$Mn$_{1-y}$Mg$_y$O$_2$ (y = 0.0, 0.05, 0.1) cathodes. Since a good understanding of the structure–composition–property relationship is key to devising better electrodes, the electrochemical performance and structural stability of the Na$_{2/3}$Mn$_{1-y}$Mg$_y$O$_2$ series of compounds are carefully monitored as a function of Mg content (y), using a combination of diffraction and solid-state NMR techniques. The electrochemical performance of the y = 0.05 cathode is exceptional, the material exhibiting very stable electrochemistry upon extended cycling and one of the highest rate performance observed to date for this class of materials.

[a] Department of Chemistry, University of Cambridge, Cambridge CB2 1EW, UK. E-mail: cpg27@cam.ac.uk

[b] School of Chemistry, University of St. Andrews, St. Andrews, Fife KY16 9ST, UK

[c] CIC ENERGIGUNE, Parque Tecnológico de Álava, Albert Einstein 48, ED. CIC, 01510 Miñano, Spain

[d] Department of Materials, University of Oxford, Oxford OX1 3PH, UK

† Electronic supplementary information (ESI) available. See DOI: 10.1039/c6ee01750a

1. Introduction

The growing demand for portable energy has driven the search for new electrode materials for rechargeable battery applications. Lithium-ion batteries (LIBs) have so far been preferred to their sodium-ion counterparts for their higher energy density

3240 | *Energy Environ. Sci.,* 2016, **9**, 3240–3251

This journal is © The Royal Society of Chemistry 2016

and operating voltages,[1] but concerns about Li supply and its rising cost have encouraged the scientific community to turn its attention to the more sustainable sodium-ion batteries (NIBs).[2–8] The latter have until recently received little attention, leaving room for the exploration of new energy storage materials. Due to the abundance and low cost of Na, NIBs are considered for grid storage applications, and could be major players in next-generation low-carbon energy technologies and in the promotion of sustainable global economic growth.

Sodium transition metal oxides (Na_xTMO_2, TM = transition metal) are well-suited for electrochemical energy storage applications as the Na^+ ions can be reversibly removed (deintercalated) from or reinserted (intercalated) into the two dimensional layered structure when the electrochemical cell is charged and discharged, respectively.[9–12] One of the major challenges faced by this particular class of materials are phase transformations occurring upon Na extraction and reinsertion.[13] Such phenomena can result in poor reversibility upon extended cycling and are characterized by staircase-like voltage profiles.[14]

Mn has a high earth-abundance and low toxicity, making Na_xMnO_2 derivatives excellent candidates for safe, low cost, sustainable cathodes. Paulsen and Dahn investigated the structural properties and phase stability of sodium manganese bronzes based on P2-type $Na_{2/3}MnO_2$ (where P2 indicates that the Na^+ ions are in trigonal prismatic sites (P), while the Mn ions are in octahedral sites, and that the O^{2-} layer stacking is AB AB (2)[15]) and of their lithium analogs obtained by ion exchange. They showed that the substitution of Mn by Li, Ni or Co reduced and eventually suppressed the Jahn–Teller distortions present in the initial $Na_{2/3}MnO_2$ structure, and extended the stability range of the P2 phase.[16] Since then, a large number of studies have looked at the substitution of the Jahn–Teller distorted Mn^{3+} ions by various transition metals in P2-type sodium transition metal oxides, as discussed in our recent review paper.[17] For instance P2-$Na_{2/3}Fe_{1/2}Mn_{1/2}O_2$ exhibits good discharge capacities on cycling up to 4.0 V, but its capacity retention is drastically reduced upon cycling up to 4.3 V due to a phase transition at high voltage.[18–20] Johnson and coworkers showed that Li substitution in the transition metal layer of P2-type $Na_xNi_yMn_zO_2$ compounds prevents the unfavorable phase transformation to the O2 phase induced by oxygen layer glides during electrochemical cycling.[21] Smooth charge/discharge curves have been obtained for $Na_{0.85}[Li_{0.17}Ni_{0.21}Mn_{0.64}]O_2$ and $Na_{0.8}[Li_{0.12}Ni_{0.22}Mn_{0.66}]O_2$,[21,22] in contrast to the staircase-like profile reported for the analogous P2-$Na_{2/3}Ni_{1/3}Mn_{2/3}O_2$ compound.[23,24] A recent study showed that Mg-substituted P2-$Na_{2/3}Mn_{2/3}Ni_{1/3-y}Mg_yO_2$ cathodes exhibit sloping electrochemical profiles (particularly for $y \geq 0.1$), no high voltage P2 to O2 phase transition, an improved cycling stability and a higher rate performance as compared with the undoped compound.[25]

The present study has been motivated by recent reports which suggest that Mg substitution for Mn in P2-type Na_xMnO_2 cathodes leads to smooth electrochemical profiles,[26] enhanced Na-ion conduction,[27] and high reversible capacity.[28] In a preliminary electrochemical study on the P2-$Na_xMn_{1-y}Mg_yO_2$ (y = 0.0, 0.05, 0.10) series, we observed high capacities and good

capacity retention upon extended cycling and at high discharge rates for the Mg-doped compounds.[29] Some of us recently reported on the influence of the applied discharge current on the structural evolution of $Na_{0.67}Mn_{0.8}Mg_{0.2}O_2$.[30] Given the lack of a detailed investigation of the dependence of the structural and electrochemical properties of P2-$Na_xMn_{1-y}Mg_yO_2$ cathodes on the Mg dopant (y) and Na (x) contents, we carry out here a comparative analysis on three different compositions: $Na_xMn_{1-y}Mg_yO_2$ (y = 0.0, 0.05, 0.10). A combination of long-range (powder X-ray, neutron, and synchrotron diffraction) and short-range (solid-state nuclear magnetic resonance) structural techniques are employed *ex situ* to characterize the evolution of the layered framework upon electrochemical cycling at the macroscale and microscale. We show that low levels of Mg substitution in P2-$Na_{2/3}MnO_2$ lead to a significant enhancement of the electrochemical properties and delay the end-of-charge phase transformation. In particular, we find that the 5% Mg-doped compound exhibits exceptional electrochemical performance, with a very high rate capability comparable to the highest reported to date on P2-type Na-ion battery cathode materials,[31] and excellent structural stability.

2. Experimental

2.1. Synthesis

Na_xMnO_2 samples ($0.6 \leq x \leq 0.7$) were prepared by solid-state synthesis. Appropriate amounts of Na_2CO_3 (Sigma Aldrich, anhydrous $\geq 99.5\%$) and Mn_2O_3 (Alfa Aesar, 99%) were ground under acetone using an agate mortar and pestle. The powder was then pelletized and calcined at 1000 °C for 15 hours in air, followed by quenching to room temperature. Various $Na_{2/3}Mn_{1-y}Mg_yO_2$ samples (with y = 0.05 and 0.1) were prepared *via* a co-precipitation method. Stoichiometric amounts of $Mn(CH_3COO)_2 \cdot 4H_2O$ and $Mg(CH_3COO)_2 \cdot 4H_2O$ (both Aldrich) were dissolved in distilled water. In a separate container, a solution of Na_2CO_3 (Fisher) was dissolved in H_2O. Co-precipitation was initiated by adding the acetate mixture dropwise to the Na_2CO_3 solution while stirring vigorously. H_2O was removed by rotary evaporation and the resulting solid was dried at 300 °C for 15 hours in air. Pellets were pressed, calcined at 600 °C for 15 hours in air, quenched, ground, pelletized again and final calcination was performed at 800 °C for 15 hours in air, followed by a quench. After the heat treatment the samples were transferred to an Ar-filled glovebox for further handling.

2.2. Electrochemistry

The electrochemical performance of $Na_{2/3}Mn_{1-y}Mg_yO_2$ (y = 0.0, 0.05, 0.10) was evaluated at room temperature. Powder samples (AM) were mixed with carbon black (CB) and polyvinylidene fluoride (PVDF) in a wt% ratio AM:CB:PVDF of 75:15:10. A slurry of the composite material was made using *N*-methyl-2-pyrrolidone (NMP). The components were pre-ground using a mortar and pestle and the mixture was stirred for 2–4 h prior to casting. The slurry was coated on a 50 μm thick aluminum foil using a doctor blade. The cast thickness of the film was

approximately 30 µm (before pressing). The coated foil was dried at 120 °C for two hours under vacuum. Electrodes were punched and pressed under a load of ~ 4 tons cm^{-2}. The active material mass loading was approximately 5 mg cm^{-2}. After compression, the electrodes were dried in vacuum overnight. They were then transferred to an Ar-filled glovebox in which O_2 and H_2O levels are maintained below 1 ppm. CR2032 coin cells were made inside the glovebox using 1 M NaClO$_4$ in EC:PC as electrolyte, Na metal as counter electrode, and Whatman® glass-fiber filter paper as separator. The cells were charged/discharged galvanostatically at different current rates using a Maccor® battery tester. Samples for diffraction and NMR measurements were prepared as pellets of combined active material, super S carbon and Kynar Flex 2801 (a co-polymer based on PVDF) binder in a mass ratio of 75:18:7. After cycling at a rate of 10 mA g^{-1}, the cells were transferred to an Ar-filled glovebox before opening and extracting the active material. The electrodes were then rinsed with a small amount of dry solvent to remove residual electrolyte and binder. They were left under dynamic vacuum overnight to ensure all solvent had evaporated. The sample powders were then transferred to capillaries/NMR rotors.

2.3. Diffraction

Powder X-ray diffraction measurements were performed on a Stoe STADI/P diffractometer operating in capillary mode, with FeKα$_1$ radiation (λ = 1.936 Å) to eliminate Mn fluorescence. Samples were loaded in 0.5 mm glass capillaries and data were collected overnight. Synchrotron powder X-ray diffraction data were obtained on the same capillaries using the I11 diffractometer at the Diamond Light Source, UK. Time-of-flight powder neutron diffraction data for selected compositions were obtained using 2 mm quartz capillaries on the Polaris instrument at ISIS at the Rutherford Appleton Laboratory, UK. Rietveld refinements of the structures were carried out using the program Topas Academic.[32]

2.4. ^{23}Na solid-state nuclear magnetic resonance (NMR)

All NMR experiments were performed under 60 kHz magic angle spinning (MAS), using a 1.3 mm double-resonance HX probe. ^{23}Na 1D spin echo spectra were recorded at room temperature on a Bruker Avance III 200 wide-bore spectrometer, at a Larmor frequency of −53.0 MHz. ^{23}Na NMR chemical shifts were referenced against solid NaCl at 7.21 ppm. ^{23}Na spin echo NMR spectra were acquired using a 90° RF (radio frequency) pulse of 1 µs at 25.04 W, a 180° RF pulse of 2 µs at 25.04 W, and a recycle delay of 20 ms. The NMR sample temperature is estimated to be in the range 320–330 K due to frictional heating introduced by fast MAS (60 kHz). All NMR spectra were processed with a 1 kHz applied line broadening. Lineshape analysis was carried out using the SOLA lineshape simulation package within the Bruker Topspin software. Transverse (T_2') relaxation times were obtained from an exponential fit of the decay of the signal intensity obtained as the echo delay was increased in an NMR spin echo pulse sequence. The fits and statistical analyses of the relaxation data were performed in MATLAB using an

in-house program written by Prof. Andrew J. Pell. The error bars depicted in Fig. 10 represent the 95% confidence intervals for the plotted T_2' values. Longitudinal (T_1) relaxation times were determined with an inversion-recovery NMR experiment. The T_1 measurements confirmed that a recycle delay of 20 ms used in the spin echo experiments was long enough for the bulk magnetization to return to equilibrium between the RF pulses.

3. Results and discussion

Electrochemical data obtained on the Na$_{2/3}$Mn$_{1-y}$Mg$_y$O$_2$ (y = 0.0, 0.05, 0.10) phases, complementary to that reported in our earlier work,[29] are presented below. In order to understand the effect of Mg doping on the structural and electronic behavior of P2-Na$_x$MnO$_2$ upon sodium extraction and reinsertion, various compositions on the first electrochemical cycle of the undoped, and 5 and 10% Mg-doped phases were investigated using a range of structural techniques.

3.1. Electrochemical performance of Na$_{2/3}$Mn$_{1-y}$Mg$_y$O$_2$ (y = 0.0, 0.05, 0.10)

3.1.1. Comparison of the overall performance of the three compounds. The overall performance of the Na$_{2/3}$Mn$_{1-y}$Mg$_y$O$_2$ (y = 0.0, 0.05, 0.10) compounds is evaluated on the basis of four major aspects of the electrochemistry: smooth charge/discharge curves, small cell polarization, and high capacity and cycle life of the electrodes at low and high cycling rates.

Plots of the differential capacity vs. voltage are shown in Fig. 1a for the various samples, and their charge/discharge curves are shown in Fig. 1b, for the second cycle, since this allows the electrochemistry for the full range of sodium stoichiometries to be explored (Fig. 1). The first cycle electrochemical data are shown in Fig. S1 in the ESI.†

A number of sharp, low intensity peaks are observed in the differential capacity vs. voltage curve (Fig. 1a) of the undoped (y = 0.0) phase, but do not appear after Mg substitution for Mn. These peaks correspond to charge ordering and structural transitions resulting from the Jahn–Teller activity of Mn^{3+} ions in the as-synthesized compounds, as previously reported for related Na$_x$MnO$_2$ phases.[11,14,33,34] For all three compositions, the oxidation and reduction peaks present at ca. 3.5 V and 3.0 V, respectively, are assigned to a reversible phase transition discussed in more detail in the later sections. Additional oxidation and reduction peaks for the undoped sample at ca. 3.7 V and 3.5 V, respectively, are assigned to a Na$^+$ ion/vacancy ordering phenomenon. A shift is observed in the end-of-discharge peak position, presumably due to different reaction mechanisms occurring at the end of discharge upon Mg doping.

As reported previously,[29] the electrochemical profiles of the Mg-doped samples, shown in Fig. 1b, are smoother than that of the undoped sample. Below 3.5 V, the Mg-doped compounds exhibit a largely sloping electrochemical profile when Na is inserted and extracted from the material. Upon galvanostatic cycling, the Mg-doped samples show a smaller hysteresis and
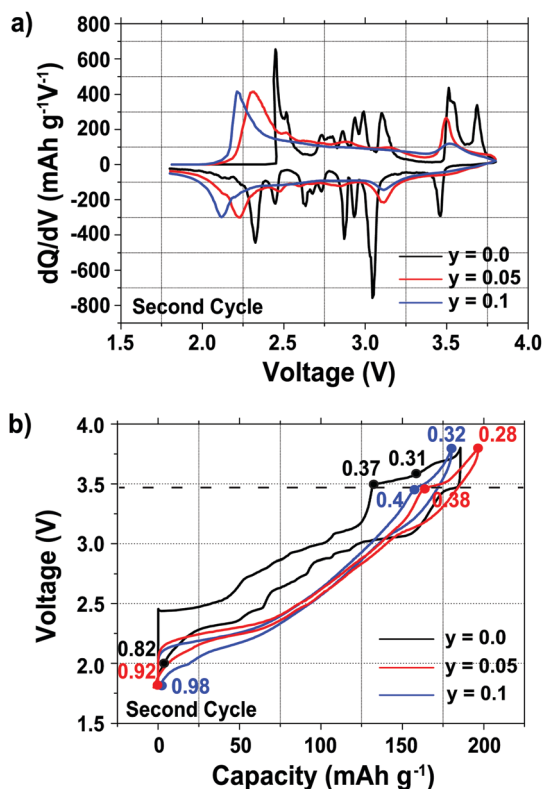
3242 | Energy Environ. Sci., 2016, **9**, 3240–3251

This journal is © The Royal Society of Chemistry 2016

Fig. 1 (a) Differential capacity *vs.* voltage plots, and (b) electrochemical profiles of the $Na_{2/3}Mn_{1-y}Mg_yO_2$ (*y* = 0.0, 0.05 and 0.1) compositions. The compounds were cycled at 10 mA g^{-1} between 1.8 and 3.8 V *vs.* Na$^+$/Na. The electrochemical cells were stopped at different points indicated on the charge/discharge curves to collect the *ex situ* diffraction data (the numbers on the curves correspond to the Na content, *x*, at which the cells were stopped). The dotted line at *ca.* 3.5 V indicates the voltage above which a phase transformation occurs in all compositions. The second cycles are shown in order to observe the electrochemical processes occurring below the open circuit voltage (OCV) of the as-synthesized materials, at *ca.* 2.5 V *vs.* Na$^+$/Na.

end-of-charge polarization, reflected in the decrease in the potential difference between the oxidation and reduction peaks in the differential capacity plots (Fig. 1a), than the undoped sample.

At a low cycling rate of 12 mA g^{-1} the initial capacity of the *y* = 0.1 phase is lower than that of the *y* = 0.0 and 0.05 compounds (see Fig. S2 in the ESI†), yet Mg doping improves the cycling stability after 25 cycles, as discussed in our earlier work.[29] The rate capability of the $Na_{2/3}Mn_{1-y}Mg_yO_2$ (*y* = 0.0, 0.05, 0.10) samples was further investigated in SCFD (slow charge fast discharge) mode, by testing cells at discharge currents of 100, 200, and 500 mA g^{-1}, while keeping the charging current constant at 12 mA g^{-1}, as shown in Fig. 2. The *y* = 0.0 compound exhibits fairly stable cycling behavior at all rates investigated. At high rates of discharge, the discharge capacity of the Mg-substituted samples is noticeably higher than for the undoped compound. At a discharge rate of 500 mA g^{-1}, for example, discharge capacities of 110, 140 and 135 mA h g^{-1} are observed after 50 cycles for the *y* = 0.0, 0.05 and 0.1 compositions, respectively. At this high Na insertion rate (500 mA g^{-1}), the 5% Mg-doped composition exhibits remarkable capacity

retention (almost 100%) with a high discharge capacity of 140 mA h g^{-1} (62% of the theoretical capacity). By comparison, only 45% of the theoretical capacity is retained after 50 cycles for the *y* = 0.0 composition.

The rate capability and cycling ability reported here for the *y* = 0.05 and 0.1 compounds cycled between 1.5 and 4.0 V are higher than those reported by Yabuuchi *et al.* for the *y* = 0.22 material cycled between 1.5 and 4.4 V.[28] The poorer rate and cycling performance for the *y* = 0.22 phase may result from the kinetically slow phase transformation in the high voltage region (>4.0 V) not explored in the present work.

3.1.2. Very high rate performance of the 5% Mg-doped material. Given the highly stable cycling performance of the *y* = 0.05 compound at a high discharge rate of 500 mA g^{-1} (see Fig. 2b), the rate performance for this material was investigated further in SCFD mode using very high discharge rates up to 10 000 mA g^{-1}.

The rate performance of the 5% Mg-doped compound, shown in Fig. 3, is exceptional. When discharge rates of 100 mA g^{-1} (~0.6C), 1000 mA g^{-1} (~6C), and 2000 mA g^{-1} (~11.5C) are applied, initial discharge capacities of *ca.* 170, 146, and 135 mA h g^{-1}, respectively, are observed. A 106 mA h g^{-1} reversible capacity is observed when a very high discharge rate of 5000 mA g^{-1} (28.6C) is applied.[31] Note that at these high rates, further electrode optimization is generally required in order to obtain improved rate performance. The rate capability of $P2-Na_{2/3}Mn_{0.95}Mg_{0.05}O_2$ is close to the highest rate performance ever reported for a P2-type cathode, namely, $P2-Na_{2/3}Mn_{1/2}Fe_{1/4}Co_{1/4}O_2$ with a 128 mA h g^{-1} reversible capacity at a 30C discharge rate.[31] Unlike Co-containing compounds (which generally exhibit high rate capabilities[31,35,36]), the materials in the present study are composed of cheap, abundant and non-toxic elements, a significant advantage for large-scale applications.

As suggested by Sharma *et al.* for the 20% Mg-doped phase, the decrease in capacity observed at very high rates of 5000 and 10 000 mA g^{-1} may be related to a lower utilization of the cathode material at the end of discharge.[30] For the 20% Mg-doped compound, a drop in reversible capacity occurs as the discharge rate is increased from 100 to 400 mA g^{-1}. A lower Mg content *y* = 0.05 results in a higher rate capability, which demonstrates that rate performance does not increase linearly with Mg content. We return to discuss the reasons for the good performance of the 5% Mg doped compound at the end of the paper, once a better understanding of the structural changes occurring in the various materials upon electrochemical cycling has been obtained.

3.2. Structural evolution of the $Na_{2/3}Mn_{1-y}Mg_yO_2$ (*y* = 0.0, 0.05, 0.10) compounds upon cycling

The long-range structural evolution of $Na_xMn_{1-y}Mg_yO_2$ (*y* = 0.0, 0.05, 0.10) upon cycling was monitored by *ex situ* powder X-ray, synchrotron X-ray, and neutron diffraction. The Na local environments in all three compositions were probed using *ex situ* ssNMR spectroscopy.

3.2.1 Na_xMnO_2

3.2.1.i. Powder XRD and Neutron diffraction results. As-prepared $Na_{2/3}MnO_2$ lies on a plateau at 2.4 V (Fig. 1b) and is composed of a

Fig. 2 Evolution of the discharge capacity as a function of the cycle number for $Na_{2/3}Mn_{1-y}Mg_yO_2$: (a) $y = 0.0$; (b) $y = 0.05$; and (c) $y = 0.1$. The cells were cycled between 1.5 and 4.0 V vs. Na^+/Na, charged at 12 mA g^{-1} and discharged at various rates, as indicated.

Fig. 3 Cycling performance of the 5% Mg-doped $Na_{2/3}Mn_{0.95}Mg_{0.05}O_2$ cathode, evaluated at various discharge rates. The cells were cycled between 1.5 and 4.0 V vs. Na^+/Na, charged at 13 mA g^{-1} and discharged at various rates, as indicated.

mixture of two phases with lower and higher sodium contents. Rietveld refinement of the diffraction pattern indicates the presence of an orthorhombic phase (space group $Cmcm$) and of a monoclinic phase (space group $C2/n$) in a 70 : 30 ratio, as shown in Fig. S3 and Table S1 in the ESI.† These two very similar phases are distorted forms of the ideal hexagonal P2 structure (space group $P6_3/mmc$). The distortion is induced by the presence of Jahn–Teller active Mn^{3+} ions and denoted by a prime (i.e. P2′).[15] In view of the two-phase behavior noted for $x = 2/3$, a range of different compositions were synthesized in an attempt to prepare a single-phase material. A single monoclinic ($C2/n$) phase was obtained when using a Na stoichiometry corresponding to $x = 0.62$ (Fig. S4 and Table S2 in the ESI†).

At the beginning of charge, the monoclinic distortion disappears and is replaced by an orthorhombic phase, as illustrated by the $Na_{0.37}MnO_2$ sample obtained after charging the material to 3.5 V vs. Na^+/Na (Fig. S5a and Table S3a in the ESI†). The expansion of the c lattice parameter (corresponding to the interlayer spacing) upon charge, observed for all $Na_{2/3}Mn_{1-y}Mg_yO_2$ ($y = 0.0, 0.05, 0.10$) phases, is due to the increase in the repulsive electrostatic interactions between adjacent MnO_2 layers as Na^+ ions are removed. Upon further Na extraction (for $x \leq 0.31$ and at potentials above 3.6 V), shearing of every other MnO_2 layer in the P2 structure (AB AB stacking) leads to the formation of an OP4 phase (AB BA CB BC stacking)[37,38] – the OP4 structure is best described in the $P6_3/mmc$ space group,[39] which converts every other prismatic layer into an octahedral layer. The $Na_{0.31}MnO_2$ compound is composed of 66% of an orthorhombic phase and 34% of an OP4 phase with a smaller c lattice parameter (Fig. S5b and Table S3b in the ESI†). At the end of charge ($x < 0.23$), only the OP4 phase is observed and most of the peaks in the X-ray diffraction pattern show considerable hkl-dependent line broadening, presumably due to deviations from the ideal OP4 stacking sequence.[29]

As Na is reinserted, the orthorhombic phase (space group $Cmcm$) gradually reappears and the OP4 phase vanishes. The sample obtained at the end of discharge, $Na_{0.82}MnO_2$, is composed of two P2′ orthorhombic phases with different Na contents: the major phase (56%) with $x = 2/3$, and the minor phase (44%) with full sodium occupancy (Fig. S5c and Table S3c in the ESI†). The latter shows a highly distorted orthorhombic structure (space group $Cmcm$). The short distance between edge- and
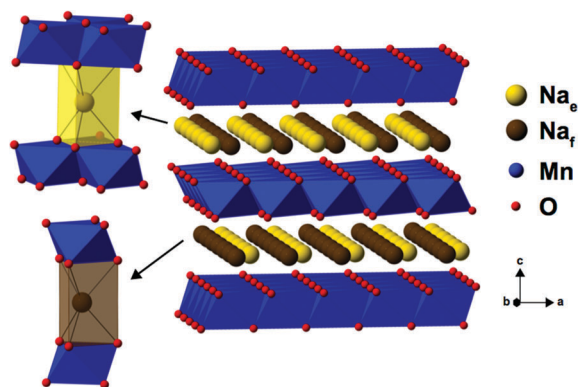
3244 | Energy Environ. Sci., 2016, 9, 3240–3251

This journal is © The Royal Society of Chemistry 2016

Fig. 4 The edge-centered (Na_e) and face-centered (Na_f) Na sites present in P2-type $Na_xMn_{1-y}Mg_yO_2$ structures.

Fig. 5 *Ex situ* ^{23}Na solid-state MAS NMR spectra collected on cells stopped at different points along the first electrochemical charge/discharge cycle of $Na_{2/3}MnO_2$, as indicated by the colored dots on the electrochemical curve on the left hand side. These and the spectra in Fig. 8a and b have been scaled according to the number of scans collected during the NMR experiment, the amount of sample in the NMR rotor, and the NMR signal decay obtained from transverse relaxation time measurements on each sample. The hash (#) indicates samples for which a lack of experimental data prevented proper scaling of the spectrum. The peak near 0 ppm is due to Na^+ ions in a diamagnetic environment, most probably from residual electrolyte or its decomposition products formed during cycling. Here and in all the ^{23}Na spectra, the asterisks (*) indicate the spinning sidebands of the main ^{23}Na NMR resonances introduced by fast rotation of the sample (MAS).

face-centered Na sites, shown in Fig. 4, means that only the former are occupied in the stoichiometric $Na_{1.0}MnO_2$ phase.

3.2.1.ii. NMR results. The spectra obtained for the undoped Na_xMnO_2 phase are presented in Fig. 5. The NMR spectrum of biphasic $Na_{2/3}MnO_2$ exhibits a number of overlapping peaks. The similarity between this and the spectrum obtained for $Na_{0.74}MnO_2$ collected on the end-of-discharge electrochemical plateau (at 2.3 V) confirms that the two phases present in the pristine sample are formed again at the end of the first electrochemical cycle. An increase in the Fermi contact shift (the main component of the overall ^{23}Na shift in paramagnetic $Na_xMn_{1-y}Mg_yO_2$ compounds) upon Mn^{3+} to Mn^{4+} oxidation has been reported in many Li/Na NMR studies of manganese-containing compounds.[40–44] We therefore assign the high frequency (1500 to 1850 ppm range) and low frequency (650 to 1150 ppm range) set of resonances to Na sites with predominantly Mn^{4+} around and with predominantly Mn^{3+} around, respectively. The low frequency, relatively sharp ^{23}Na resonance appearing at about 700 ppm when $Na_{2/3}MnO_2$ is initially discharged (see the $Na_{0.9}MnO_2$ spectrum), and after one charge/discharge cycle (see the $Na_{0.82}MnO_2$ spectrum), is in good agreement with a low average Mn oxidation state, close to +III.

As expected, the ^{23}Na NMR shift increases upon charge. The numerous electrochemical plateaus observed between $x = 2/3$ and $x = 0.31$ (*i.e.* between 2.5 and 3.5 V on charge, see Fig. 1b) are indicative of Jahn–Teller induced structural transitions, Mn^{3+}/Mn^{4+} orderings on the transition metal lattice, and/or Na^+ ion/vacancy ordering transitions in the Na layers,[11,14,33,34] and account for the complex changes observed in the ^{23}Na spectra. As the Na content drops from 0.31 to 0.23, a broad peak centered around 1100 ppm (assigned to the OP4 phase observed in the Rietveld refinements) grows at the expense of the sharper peak at higher frequencies (corresponding to the orthorhombic P2′ phase). The broadening of the NMR spectrum results from Mn^{3+}/Mn^{4+} oxidation and from partial layer shearing at low Na contents giving rise to a range of Na local environments and hence to a distribution of ^{23}Na resonant frequencies. In addition, the contraction of the structure at high voltage is likely to hamper Na-ion hopping between sites, leading to low Na-ion
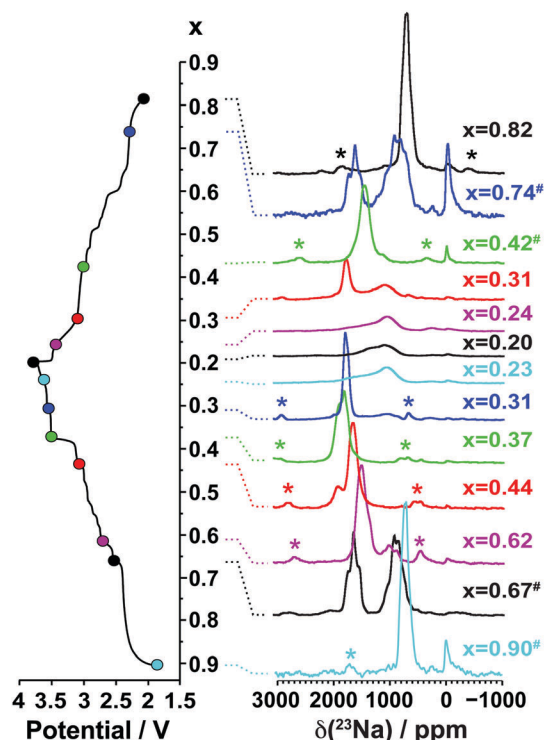
mobility and further broadening of the NMR peaks. The origin of the decrease in the ^{23}Na resonant frequency at the end of charge (from *ca.* 1800 to 1100 ppm) is discussed in the ESI.† The evolution of the NMR spectra upon discharge demonstrates the reversibility of the processes occurring upon charge.

3.2.2. $Na_xMn_{0.95}Mg_{0.05}O_2$ and $Na_xMn_{0.9}Mg_{0.1}O_2$

3.2.2.i. Synchrotron XRD and neutron diffraction results. The as-prepared P2′ $Na_{0.67}Mn_{0.95}Mg_{0.05}O_2$ and $Na_{0.67}Mn_{0.9}Mg_{0.1}O_2$ phases adopt an orthorhombic symmetry (*Cmcm* space group), as reported by Billaud *et al.*[29] Superlattice peaks are absent from the XRD data collected on the 5 and 10% Mg doped phases, suggesting no long-range ordered pattern of the Mg and Mn ions on the transition metal lattice, unlike that reported for the P2-type $Na_xMn_{0.89}Mg_{0.11}O_2$ and $Na_{0.67}Mn_{0.72}Mg_{0.28}O_2$ compounds.[26,28]

Upon charge, the structure of the 5% Mg-doped material remains orthorhombic down to $x = 0.38$ (Fig. 6a and Table S4a in the ESI†). The 10% Mg-doped compound crystallizes in the ideal P2 structure with hexagonal symmetry ($P6_3/mmc$ space group) when $x = 0.40$ (Fig. 7a and Table S7a in the ESI†), due to the smaller proportion of Mn^{3+} ions in this material (22% of all Mn).

Fig. 6 Fitted powder neutron diffraction patterns for 5% Mg-doped: (a) $Na_{0.38}Mn_{0.95}Mg_{0.05}O_2$ formed before the end-of-charge voltage plateau; (b) $Na_{0.28}Mn_{0.95}Mg_{0.05}O_2$ formed after the end-of-charge voltage plateau (upper tick marks correspond to the OP4 phase and lower tick marks to the P2 phase); and (c) $Na_{0.92}Mn_{0.95}Mg_{0.05}O_2$ obtained at the end of discharge (lower tick marks correspond to the $Na_1Mn_{0.95}Mg_{0.05}O_2$ reflections and upper tick marks to the $Na_{0.7}Mn_{0.95}Mg_{0.05}O_2$ reflections). In these and all subsequent diffraction patterns, the red dots represent the observed data and the solid line the calculated pattern; the lower line is the difference/esd; the tick marks represent the allowed reflections.

At the end of charge, the Mg-doped materials do not fully transform to the OP4 phase, unlike Na_xMnO_2. They are composed of a major P2 phase and of a minor disordered OP4 phase (also in the $P6_3/mmc$ space group), in a 60 : 40, and a 65 : 35 ratio, respectively (Fig. 6b, 7b and Tables S4b, S7b in the ESI†).

As Na is reinserted, the OP4 phase disappears. For the 5% doped compound, the $x = 0.40$ composition crystallizes in the ideal P2 structure (Fig. S6 and Table S5 in the ESI†), and a P2′ orthorhombic phase is formed upon further Na reinsertion (Fig. S7 and Table S6 in the ESI†). As the 10% doped cathode material is discharged and $x \geq 0.43$, the structure becomes and remains orthorhombic until the final stage of discharge (Fig. S8 and Table S8 in the ESI†). The Mg-doped materials exhibit a two-phase region at high Na contents ($x > 0.9$). $Na_{0.92}Mn_{0.95}Mg_{0.05}O_2$, obtained when the 5% Mg-doped material has been fully discharged, consists of a major phase (78%) with a Na stoichiometry of 1, and of a minor phase (22%) with a lower Na content (Fig. 6c and Table S4c in the ESI†). The 10% Mg-doped $Na_{0.98}Mn_{0.9}Mg_{0.1}O_2$ sample is composed of a major phase (88%) with $x = 1$, and of a minor phase (12%) with a lower Na content (Fig. 7c and Table S7c in the ESI†).

3.2.2.ii. NMR results. The ^{23}Na NMR spectra obtained for the Mg-doped ($y = 0.05, 0.1$) phases are presented in Fig. 8a and b.

Two ^{23}Na resonances, denoted as Na_I and Na_{II}, are present in the spectra of the as-synthesized $Na_{2/3}Mn_{1-y}Mg_yO_2$

($y = 0.05, 0.1$) samples. Fits of the spectra indicate a $Na_I : Na_{II}$ occupation ratio of 20 : 1 for $Na_{0.67}Mn_{0.95}Mg_{0.05}O_2$, and of 50 : 1 for $Na_{0.67}Mn_{0.9}Mg_{0.1}O_2$. The large population difference of the two environments rules out an assignment of Na_I and Na_{II} to the two crystallographic edge- and face-centered sites in the P2′ orthorhombic structure. Instead, the Na_I resonance is assigned to an average signal resulting from rapid exchange on the NMR timescale of Na^+ ions between edge- and face-centered interlayer sites in the P2′ phase (fast Na-ion motion results in coalescence of the resonances from these sites). This single, relatively sharp Na_I resonance is in stark contrast to the broad overlapping peaks observed for the $Na_{2/3}MnO_2$ phase, the latter suggesting multiple phases and slower Na-ion motion within the Na layers in the undoped material. The low frequency Na_{II} signal indicates the presence of a Mn^{3+}-rich phase. It is assigned to an O3′ α-$NaMnO_2$ impurity present in small amounts and not detected in the XRD data, as shown in Fig. S10 and discussed in more detail in the ESI.† The Na_{II} resonance disappears at early stages of charge (as soon as $x = 0.49$), suggesting Na-ion removal from the α-$NaMnO_2$ phase or domains at low voltage.

Upon Na deintercalation, the ^{23}Na resonances shift towards higher frequencies, as noted previously for the undoped material (see Fig. 5). Mg doping, however, leads to more continuous changes in the Na resonances, and to fewer, sharper peaks throughout the first electrochemical cycle (when $x \leq 2/3$). These observations,
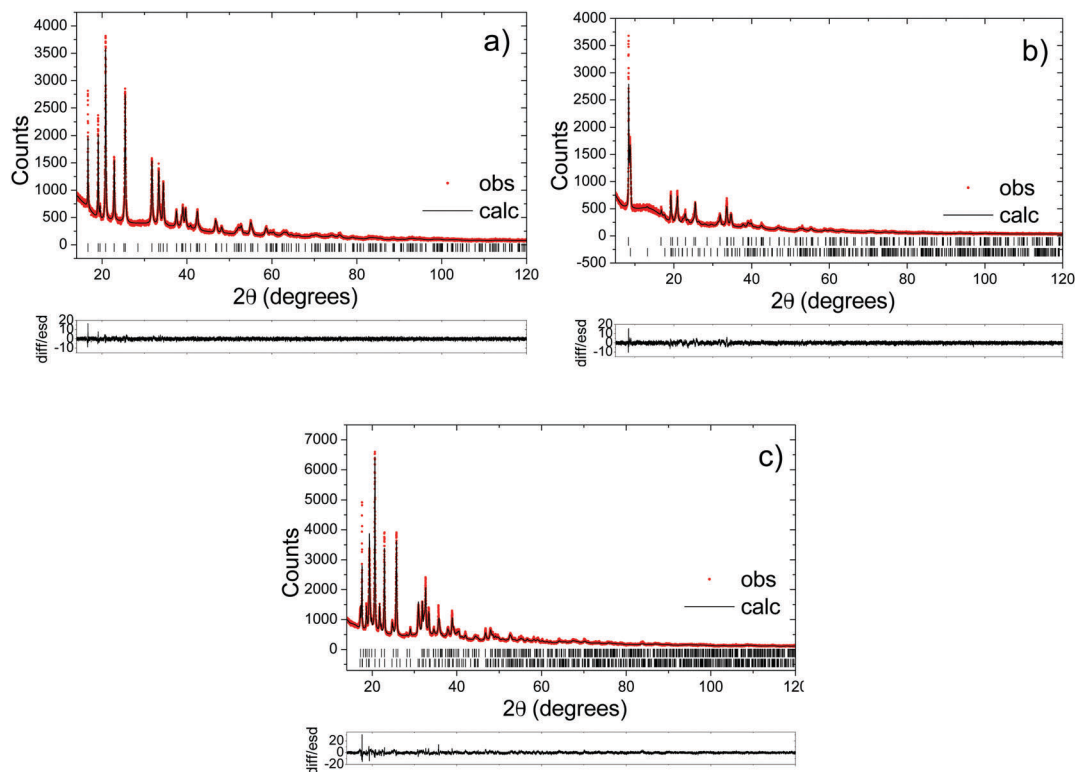
3246 | *Energy Environ. Sci.*, 2016, **9**, 3240–3251

This journal is © The Royal Society of Chemistry 2016

Fig. 7 Fitted synchrotron diffraction patterns for 10% Mg-doped: (a) $Na_{0.40}Mn_{0.9}Mg_{0.1}O_2$ formed before the end-of-charge voltage plateau; (b) $Na_{0.32}Mn_{0.9}Mg_{0.1}O_2$ formed after the end-of-charge voltage plateau (upper tick marks correspond to the P2 phase and lower tick marks to the OP4 phase); and (c) $Na_{0.98}Mn_{0.9}Mg_{0.1}O_2$ obtained at the end of discharge (lower tick marks correspond to the $Na_1Mn_{0.9}Mg_{0.1}O_2$ reflections and upper tick marks to the $Na_{0.7}Mn_{0.9}Mg_{0.1}O_2$ reflections).

together with the smoother electrochemical curves obtained upon Mg doping and the XRD data presented earlier, suggest more gradual electronic and structural changes upon Na (de)intercalation. Unlike in Na_xMnO_2, there is no evidence from NMR and XRD data for Na^+ ion/vacancy and/or Mn^{3+}/Mn^{4+} ordering transitions upon charge of the 10% Mg-doped compound. The spectra obtained on the $Na_{2/3}Mn_{1-y}Mg_yO_2$ (y = 0.05, 0.1) phases charged to 3.8 V indicate that the proportion of Na^+ ions in OP4 distorted prismatic edge-centered sites, with a shift around 1100 ppm, decreases as the Mg doping level is increased from 5 to 10%. In principle, the 1100 ppm resonance could result from O2 stacking faults within the P2 phase, however, the OP4 phase is observed by XRD for all Mg substitution levels, consistent with the assignment of the 1100 ppm resonance to this phase rather than to an environment within a disordered P2 phase.

The evolution upon electrochemical cycling of the ^{23}Na transverse (T_2') NMR relaxation time is shown in Fig. 9 for $Na_{2/3}Mn_{1-y}Mg_yO_2$ (y = 0.0, 0.05, 0.1). The two T_2' values recorded at certain Na compositions correspond to two different phases: the P2 and OP4 phases in the end-of-charge samples, and the two P2′ phases with different Na contents in the end-of-discharge samples. For $2/3 \geq x > 0.3$, very short transverse relaxation times, in the range of 33 to 112 μs, are obtained for the Mg-doped phases. Li-ion motion on the timescale of μs to ms has recently been shown to be a major source of fast T_2'

relaxation (short relaxation times) in lithium-containing paramagnetic cathodes.[45] By analogy, we ascribe the short ^{23}Na T_2' times to rapid Na-ion hopping between edge- and face-centered prismatic sites in the P-type layers. The range of Na compositions over which transverse relaxation is fast is reduced for Na_xMnO_2, in agreement with the various ordering and structural transitions occurring upon cycling and affecting fast Na-ion conduction.

Long T_2' relaxation times (>2.0 ms) are recorded for the discharged Na_xMnO_2 samples. The broad resonances observed in the spectra collected on the biphasic 5 and 10% Mg-doped end-of-discharge ($x \geq 0.92$) samples (see Fig. 8a and b) result from a combination of frequency overlap between the signals assigned to the two phases and a spread in the ^{23}Na resonant frequencies due to a range of TM–TM (and TM–O) bond distances in the severely Jahn–Teller distorted phases.[18] The two phases have very different T_2' relaxation behaviors. The slow relaxing component ($T_2' > 0.5$ ms) is assigned to rigid Na^+ ions in the orthorhombically-distorted $x = 1.0$ phase, leading to further broadening of the spectra. The faster relaxing component is assigned to the more mobile Na^+ ions in the second phase with a lower Na content.

At the end of charge, broad resonances and increased T_2' relaxation times (0.8–1.0 ms) are recorded for the 0 and 5% Mg-doped materials. The broad spectra are due to partial layer shearing and increased structural disorder at short
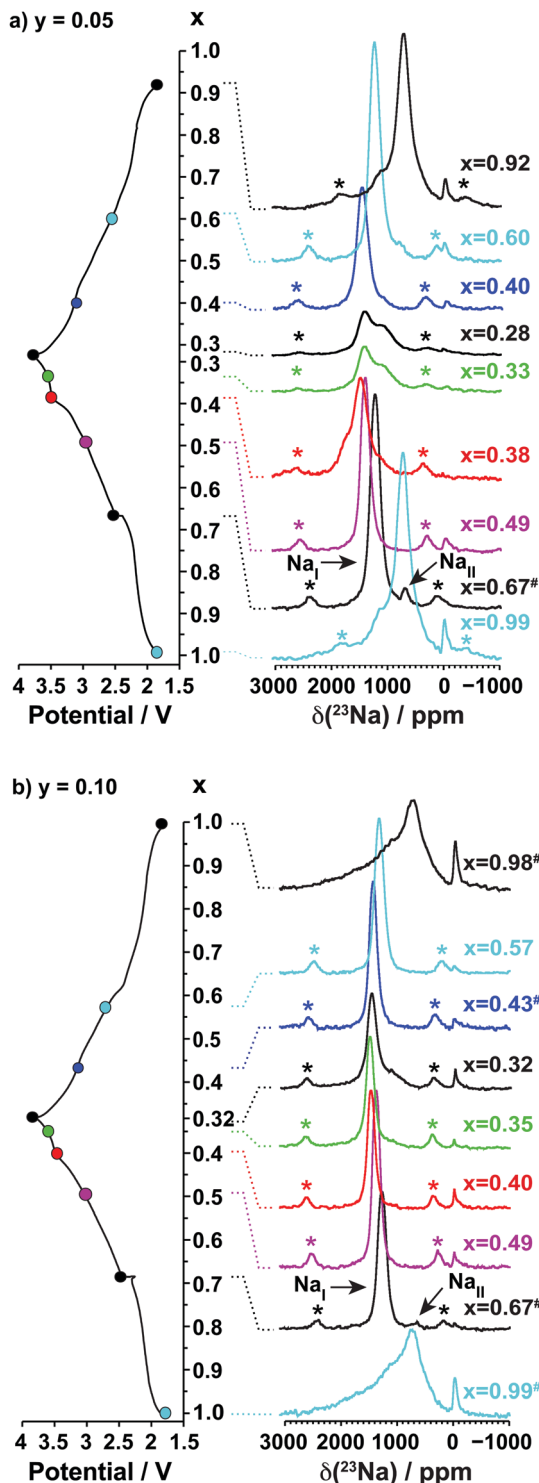
Fig. 9 Plot of the transverse NMR relaxation time (T_2') obtained on samples at different points along the first electrochemical charge/discharge cycle of $Na_{2/3}Mn_{1-y}Mg_yO_2$ (y = 0.0, 0.05, 0.1) as a function of Na content (x). Two relaxation times are plotted on the graph when two phases or local environments were identified in the sample. Error bars for the determination of the T_2' values represent the 95% confidence intervals.

1100 ppm (see Fig. 5 and 8a). 10% Mg substitution leads to significant improvements in Na-ion mobility up to 3.8 V charge, demonstrated by narrow ^{23}Na NMR peaks and transverse relaxation times below 112 µs throughout cycling (for $x \leq 2/3$).

3.3. How does Mg doping improve the structural and electrochemical properties of P2-$Na_{2/3}MnO_2$?

Fig. 10 summarizes the structural evolution of $Na_xMn_{1-y}Mg_yO_2$ (y = 0.0, 0.05, 0.1) as a function of Na content (x), as inferred from Rietveld refinements on different samples obtained by electrochemical Na extraction/insertion presented in this paper, in the ESI† or in our previous study.[29] While structures with an orthorhombic and/or monoclinic P2′ distortion (shown as orange and green squares, respectively) are generally observed at higher Na contents, hexagonal P2 structures (blue squares) and OP4 phases (red squares) are obtained for $x \leq 0.44$.

3.3.1. A higher average Mn oxidation state for a given Na content. For a given Na content, say x = 2/3, Mg substitution raises the average Mn oxidation state from 3.33 in the undoped material to 3.40 and 3.48 in the 5 and 10% Mg-doped compounds. Consequently, the Mg-doped phases have a more Na-rich composition at the low voltage cut-off. The higher Na content at the low voltage cut-off compensates for some of the loss of capacity due to the introduction of electrochemically-inactive Mg leading to a higher Na content at the high voltage cut-off. In other words, the Na composition range has been shifted to a higher Na content for the same range of Mn oxidation states (*i.e.* the range between the low and high voltage cut-offs).

3.3.2. Extending the range of solid-solution behavior. Irrespective of Mg content, Mn^{3+}-induced cooperative Jahn–Teller distortions at high Na contents ($x \geq 0.82$) result in oxidation/reduction peaks in the 2.2–2.4 V range in the dQ/dV plots in Fig. 1a and in the stabilization of an orthorhombically-distorted x = 1 P2′ phase (see Fig. 10). The end-of-discharge structures are highly distorted at the local level, as demonstrated by the broad resonances in the ^{23}Na NMR spectra (see Fig. 8a and b). The presence of Mg extends the region of solid-solution behavior and limits the biphasic domain to Na contents $x > 2/3$,

Fig. 8 *Ex situ* ^{23}Na solid–state MAS NMR spectra collected on cells stopped at different points along the first electrochemical charge/discharge cycle of $Na_{2/3}Mn_{1-y}Mg_yO_2$: (a) y = 0.05, and (b) y = 0.10, as indicated by the colored dots on the electrochemical curve on the left hand side of the spectra. The peak near 0 ppm is due to Na^+ ions in a diamagnetic environment, most probably from residual electrolyte or its decomposition products formed during cycling.

length scales, as well as overlap between the residual P2 resonance around 1450 ppm, and the OP4 resonance around
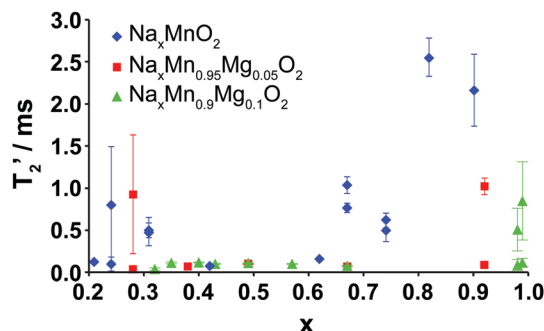
3248 | *Energy Environ. Sci.*, 2016, **9**, 3240–3251

This journal is © The Royal Society of Chemistry 2016

Fig. 10 Ranges of P2, P2′ and OP4 phase stability for $Na_xMn_{1-y}Mg_yO_2$ (y = 0.0, 0.05, 0.1) upon electrochemical Na removal and reinsertion, obtained from Rietveld refinements of diffraction data. The ideal hexagonal P2 phase is depicted in blue, the OP4 phase in red, and the Jahn−Teller distorted P2′ phases are depicted in green (monoclinic distortion) and orange (orthorhombic distortion). When more than one phase is observed, $e.g.$ for the 10% Mg-doped material at x = 0.98 composed of two orthorhombic phases, two squares are shown above and below the x axis.

while as-prepared $Na_{2/3}MnO_2$ consists of two phases (see Fig. 10) and lies on a voltage plateau at $ca.$ 2.4 V.

By increasing the average Mn oxidation state, $i.e.$ by reducing the number of Jahn–Teller active ions in P2 Na_xMnO_2, Mg doping leads to more gradual and more reversible structural and electronic changes upon cycling, as indicated by diffraction and NMR results. Sloping profiles are obtained at the beginning of charge and up to 3.5 V for the Mg-doped compounds (see Fig. 1).

3.3.3. Preventing Mn^{3+}/Mn^{4+} and Na^+ ion/vacancy ordering transitions upon cycling. Na^+ ion/vacancy ordering has been reported at particular Na stoichiometries in Na_xMnO_2 compounds,[11,14,33,34] and can be a significant obstacle to fast Na-ion motion.[46,47] Na^+ ion/vacancy superstructures result from the interplay between the repulsive Na^+–Na^+ interactions, Na^+–TM^{n+} interactions, and from $TM^{n+}/TM^{(n+1)+}$ charge ordering on the transition metal lattice. The lack of superstructure peaks in the XRD patterns of the $Na_{2/3}Mn_{1-y}Mg_yO_2$ (y = 0.05, 0.1) phases suggests that Mg and Mn cations are disordered. Furthermore, the presence of Mg on the transition metal lattice disrupts Mn^{3+}/Mn^{4+} charge ordering. The present work confirms that low concentrations (5%) of spectator ions in the transition metal lattice, here Mg^{2+}, can effectively prevent Na^+ ion/vacancy ordering in $P2-Na_xTMO_2$ compounds, as has been observed in $P2-Na_{2/3}Mn_{2/3}Ni_{1/3-y}Mg_yO_2$ compounds[25] and upon Ti^{4+} doping in $P2-Na_{0.6}Cr_{0.6}Ti_{0.4}O_2$.[48]

3.3.4. Limiting layer shearing at high voltage. Partial shearing of the TMO_2 layers at low Na contents is commonly observed in $P2-Na_xTMO_2$ compounds, giving rise to a new phase containing O-type layers or stacking faults.[18–20,22,26,39,49] Layer shearing counterbalances the increase in electrostatic repulsions between oxygen anions from adjacent TMO_2 slabs at low Na contents. Here, an OP4 phase forms in the end-of-charge $Na_xMn_{1-y}Mg_yO_2$ samples. The remaining Na^+ ions are located in the prismatic layers and the octahedral layers are completely vacant (Tables S3b, S4b, and S7b in the ESI†).

The extent of layer shearing at high voltage depends on the number of remaining Na^+ ions holding the MnO_2 layers together.

As shown in Fig. 10, the P2 to OP4 phase transformation occurs around x = 0.31–0.33, irrespective of Mg content. In the undoped material, complete phase transformation to the OP4 phase occurs by 3.6 V, when x < 0.24. In the 5 and 10% Mg-doped compounds, with an end-of-charge Na content of 0.28 and 0.32, respectively, the frequency of layer shearing events is reduced and partial P2 to OP4 phase transition takes place at a higher potential.

The P2 to OP4 phase transformation leads to oxidation peaks above 3.5 V in the electrochemical dQ/dV curves (Fig. 1a) and to a rise in the overpotential of the cell, because of the activation barrier associated with the phase transition process. The decrease in the end-of-charge overpotential (Fig. 1b) is in agreement with the smaller fraction of OP4 phase formed as more Mg is doped into $P2-Na_xMnO_2$.

The formation of an OP4 phase, intermediate between the P2 and O2 layer stackings, appears to be less structurally damaging, hence more reversible, than the P2–O2 phase transition observed upon Na extraction from $e.g.$ $P2-Na_{2/3}Ni_{1/3}Mn_{2/3}O_2$.[24] By increasing the average Mn oxidation state for a given Na content and allowing Na to be extracted at higher voltage, Mg substitution delays, rather than completely prevents, O layer glides. As reported for $P2-Na_{2/3}Mn_{2/3}Ni_{1/3-y}Mg_yO_2$ compounds,[25] the stabilization of the $P2-Na_xMnO_2$ structure upon Mg doping leads to good cycling stability.

3.3.5. Superior rate performance and cycling stability upon 5% Mg doping. Previous work on related P2 cathodes has shown that end-of-discharge processes, rather than end-of-charge structural changes, are rate-limiting.[30,31] Recent work by Sharma et $al.$[30] showed that the structural evolution of $P2-Na_xMg_{0.8}Mn_{0.2}O_2$ is highly dependent on the rate of discharge. High rates inhibit the slow nucleation and growth of the $Cmcm$ phase with full Na occupancy at low potentials.[30] Here, we find that high rate performance does not increase linearly with Mg content. Instead, 5% Mg-doping leads to optimal rate performance. Ex $situ$ data obtained at slow cycling rates on the y = 0.0, 0.05, 0.1,

and 0.2 materials show that, while the $y = 0.2$ P2 phase fully transforms to a *Cmcm* phase at the end of discharge,[30] lower Mg contents lead to a two-phase regime at high Na contents (see Fig. 10). The proportion of *Cmcm* phase with full Na occupancy (and with a slower Na-ion conductivity compared to the second phase with a lower Na content, see Fig. 9) increases with Mg content: from 44% in the undoped material, to 78 and 88% in the 5 and 10% Mg-doped compounds, respectively. These observations suggest that the optimal rate performance observed for $y = 0.05$ results from: (1) TM and Na$^+$ ion/vacancy disorder in the layers, fostered by the presence of Mg^{2+} ions; and (2) the presence of a small fraction (22%) of a P2$'$ phase with high Na conduction properties in the end-of-discharge material, which decreases with Mg content. It is important to note that the *ex situ* diffraction and ^{23}Na ssNMR results presented here describe the relaxed Na$_x$Mg$_y$Mn$_{1-y}$O$_2$ structures after cycling at a slow rate of 10 mA g^{-1}, and do not reflect real time structural changes occurring at higher discharge rates. As observed for $y = 0.2$,[30] the proportion of the $x = 1$ *Cmcm* phase in the end-of-discharge $y = 0.0$, 0.05, and 0.1 materials is expected to decrease, and the proportion of the P2$'$ phase with a lower Na content is expected to increase with increasing discharge rate.

The high voltage plateau is observed at all rates explored in this work, suggesting that the partial P2 to OP4 phase transformation, which induces minimal structural changes as compared with the P2 to *Cmcm* phase transition, is not rate limiting in the 5% Mg-doped material. The exact cause for poor cycling stability in P2-type cathodes is still not clearly understood, yet it has been related to the high voltage phase transition in P2-Na$_x$Mn$_{1/2}$Fe$_{1/2}$O$_2$,[18,20,50] and in P2-Na$_x$Mn$_{1/2}$Fe$_{1/4}$Co$_{1/4}$O$_2$.[31] Here, the large polarization and hysteresis observed at high voltage (see Fig. 1b) presumably leads to capacity fade upon extended cycling (see Fig. 2), which is exacerbated at high discharge rates (see Fig. 3). As suggested for P2-Na$_x$Mn$_{1/2}$Fe$_{1/2}$O$_2$,[50] the large volume changes associated with the high voltage transition from the P2 to the OP4 phase likely contribute to structural irreversibility. Rapid expansion of the $y = 0.05$ structure when the OP4 component converts back to the P2 phase leads to poorer structural stability, hence poorer capacity retention, at very high discharge rates.

4. Conclusions

An in-depth comparative study of the electrochemical properties and structural changes occurring upon cycling of P2-type Na$_x$Mn$_{1-y}$Mg$_y$O$_2$ ($y = 0.0$, 0.05, 0.1) materials showed that low levels of Mg doping (5 and 10%) improve the electrochemical performance and structural stability of the material. While long-range structural changes were monitored using powder X-ray, neutron, and synchrotron diffraction, local changes were characterized with ^{23}Na solid-state NMR to obtain a full picture of the structural evolution of the cathode materials at both lengthscales. The presence of Mg on the transition metal lattice leads to fewer Jahn–Teller distorted Mn^{3+} ions and disrupts potential Mn^{3+}/Mn^{4+} ordering. As a result, fewer structural and

electronic processes take place as the cell is cycled and smoother load curves are obtained. In addition, the greater number of Na$^+$ ions present at the end of charge, when Mg is substituted in the compound, increases the voltage range over which the P2 phase is stable and delays the occurrence of oxygen layer glides leading to the formation of an OP4 phase. Although the theoretical capacity decreases as more electrochemically-inactive Mg is introduced into the material, the presence of Mg leads to higher capacity retention after 50 cycles at a 500 mA g^{-1} discharge rate (110 mA h g^{-1} for the undoped phase, *vs.* 140 and 135 mA h g^{-1} for the Mg doped phases). The 5% Mg-doped compound exhibits exceptional rate performance, with *ca.* 106 mA h g^{-1} initial reversible capacity observed at a 5000 mA g^{-1} discharge rate, and excellent capacity retention. Such rate performance is among the highest observed for P2-type cathode materials.

Acknowledgements

References

1 M. Armand and J.-M. Tarascon, *Nature*, 2008, **451**, 652–657.

2 S.-W. Kim, D.-H. Seo, X. Ma, G. Ceder and K. Kang, *Adv. Energy Mater.*, 2012, **2**, 710–721.

3 H. Pan, Y.-S. Hu and L. Chen, *Energy Environ. Sci.*, 2013, **6**, 2338.

4 M. D. Slater, D. Kim, E. Lee and C. S. Johnson, *Adv. Funct. Mater.*, 2013, **23**, 947–958.

5 N. Yabuuchi, K. Kubota, M. Dahbi and S. Komaba, *Chem. Rev.*, 2014, **114**, 11636–11682.

6 V. Palomares, M. Casas-Cabanas, E. Castillo-Martínez, M. H. Han and T. Rojo, *Energy Environ. Sci.*, 2013, **6**, 2312.

7 V. Palomares, P. Serras, I. Villaluenga, K. B. Hueso, J. Carretero-González and T. Rojo, *Energy Environ. Sci.*, 2012, **5**, 5884–5901.

8 M. Dahbi, N. Yabuuchi, K. Kubota, K. Tokiwa and S. Komaba, *Phys. Chem. Chem. Phys.*, 2014, **16**, 15007–15028.

9 Y. Takeda, K. Nakahara, M. Nishijima and N. Imanishi, *Mater. Res. Bull.*, 1994, **29**, 659–666.

10 S. Komaba, C. Takei, T. Nakayama, A. Ogata and N. Yabuuchi, *Electrochem. Commun.*, 2010, **12**, 355–358.

11 A. Mendiboure, C. Delmas and P. Hagenmuller, *J. Solid State Chem.*, 1985, **57**, 323–331.

3250 | *Energy Environ. Sci.*, 2016, **9**, 3240–3251

This journal is © The Royal Society of Chemistry 2016

12 M. H. Han, E. Gonzalo, G. Singh and T. Rojo, *Energy Environ. Sci.*, 2015, **8**, 81–102.

13 M. Galceran, V. Roddatis, F. J. Zúñiga, J. M. Pérez-Mato, B. Acebedo, R. Arenal, I. Peral, T. Rojo and M. Casas-Cabanas, *Chem. Mater.*, 2014, **26**, 3289–3294.

14 A. Caballero, L. Hernán, J. Morales, L. Sánchez, J. S. Peña and M. A. G. Aranda, *J. Mater. Chem.*, 2002, **12**, 1142–1147.

15 C. Delmas, C. Fouassier and P. Hagenmuller, *Physica B+C*, 1980, **99**, 81–85.

16 J. M. Paulsen and J. R. Dahn, *Solid State Ionics*, 1999, **126**, 3–24.

17 R. J. Clément, P. G. Bruce and C. P. Grey, *J. Electrochem. Soc.*, 2015, **162**, A2589–A2604.

18 B. Mortemard de Boisse, D. Carlier, M. Guignard, L. Bourgeois and C. Delmas, *Inorg. Chem.*, 2014, **53**, 11197–11205.

19 G. Singh, J. M. L. del Amo, M. Galceran, S. Pérez-Villar and T. Rojo, *J. Mater. Chem. A*, 2015, **3**, 6954–6961.

20 E. Talaie, V. Duffort, H. L. Smith, B. Fultz and L. F. Nazar, *Energy Environ. Sci.*, 2015, **8**, 2512–2523.

21 D. Kim, S.-H. Kang, M. Slater, S. Rood, J. T. Vaughey, N. Karan, M. Balasubramanian and C. S. Johnson, *Adv. Energy Mater.*, 2011, **1**, 333–336.

22 J. Xu, D. H. Lee, R. J. Clément, X. Yu, M. Leskes, A. J. Pell, G. Pintacuda, X.-Q. Yang, C. P. Grey and Y. S. Meng, *Chem. Mater.*, 2014, **26**, 1260–1269.

23 Z. Lu and J. R. Dahn, *J. Electrochem. Soc.*, 2001, **148**, A1225–A1229.

24 D. H. Lee, J. Xu and Y. S. Meng, *Phys. Chem. Chem. Phys.*, 2013, **15**, 3304–3312.

25 P. F. Wang, Y. You, Y.-X. Yin, Y. S. Wang, L.-J. Wan, L. Gu and Y.-G. Guo, *Angew. Chem.*, 2016, **128**, 7571–7575.

26 D. Buchholz, C. Vaalma, L. G. Chagas and S. Passerini, *J. Power Sources*, 2015, **282**, 581–585.

27 Z.-Y. Li, R. Gao, J. Zhang, X. Zhang, Z. Hu and X. Liu, *J. Mater. Chem. A*, 2016, **4**, 3453–3461.

28 N. Yabuuchi, R. Hara, K. Kubota, J. Paulsen, S. Kumakura and S. Komaba, *J. Mater. Chem. A*, 2014, **2**, 16851–16855.

29 J. Billaud, G. Singh, A. R. Armstrong, E. Gonzalo, V. Roddatis, M. Armand, T. Rojo and P. G. Bruce, *Energy Environ. Sci.*, 2014, **7**, 1387–1391.

30 N. Sharma, N. Tapia-Ruiz, G. Singh, A. R. Armstrong, J. C. Pramudita, H. E. A. Brand, J. Billaud, P. G. Bruce and T. Rojo, *Chem. Mater.*, 2015, **27**, 6976–6986.

31 L. Liu, X. Li, S.-H. Bo, Y. Wang, H. Chen, N. Twu, D. Wu and G. Ceder, *Adv. Energy Mater.*, 2015, **5**, 1500944.

32 A. A. Coelho, *J. Appl. Crystallogr.*, 2000, **33**, 899–908.

33 X. Li, X. Ma, D. Su, L. Liu, R. Chisnell, S. P. Ong, H. Chen, A. Toumar, J.-C. Idrobo, Y. Lei, J. Bai, F. Wang, J. W. Lynn, Y. S. Lee and G. Ceder, *Nat. Mater.*, 2014, **13**, 586–592.

34 D. Su, C. Wang, H. J. Ahn and G. Wang, *Chem. – Eur. J.*, 2013, **19**, 10884–10889.

35 Z.-Y. Li, R. Gao, L. Sun, Z. Hu and X. Liu, *J. Mater. Chem. A*, 2015, **3**, 16272–16278.

36 T. Shibata, Y. Fukuzumi, W. Kobayashi and Y. Moritomo, *Sci. Rep.*, 2015, **5**, 9006.

37 Z. Ren, J. Shen, S. Jiang, X. Chen, C. Feng, Z. Xu and G. Cao, *J. Phys.: Condens. Matter*, 2006, **18**, L379.

38 R. Balsys, *Solid State Ionics*, 1997, **93**, 279–282.

39 R. Berthelot, M. Pollet, D. Carlier and C. Delmas, *Inorg. Chem.*, 2011, **50**, 2420–2430.

40 J. Billaud, R. J. Clément, A. R. Armstrong, J. Canales-Vázquez, P. Rozier, C. P. Grey and P. G. Bruce, *J. Am. Chem. Soc.*, 2014, **136**, 17243–17248.

41 Y. J. Lee and C. P. Grey, *Chem. Mater.*, 2000, **12**, 3871–3878.

42 K. A. Aldi, J. Cabana, P. J. Sideris and C. P. Grey, *Am. Mineral.*, 2012, **97**, 883–889.

43 H. Duncan, B. Hai, M. Leskes, C. P. Grey and G. Chen, *Chem. Mater.*, 2014, **26**, 5374–5382.

44 Y. J. Lee, F. Wang and C. P. Grey, *J. Am. Chem. Soc.*, 1998, **120**, 12601–12613.

45 L. Zhou, M. Leskes, T. Liu and C. P. Grey, *Angew. Chem., Int. Ed.*, 2015, **54**, 14782–14786.

46 G. J. Shu and F. C. Chou, *Phys. Rev. B: Condens. Matter Mater. Phys.*, 2008, **78**, 052101.

47 A. J. Toumar, S. P. Ong, W. D. Richards, S. Dacek and G. Ceder, *Phys. Rev. Appl.*, 2015, **4**, 064002.

48 Y. Wang, R. Xiao, Y.-S. Hu, M. Avdeev and L. Chen, *Nat. Commun.*, 2015, **6**, 6954.

49 N. Bucher, S. Hartung, J. B. Franklin, A. M. Wise, L. Y. Lim, H.-Y. Chen, J. N. Weker, M. F. Toney and M. Srinivasan, *Chem. Mater.*, 2016, **28**, 2041–2051.

50 W. K. Pang, S. Kalluri, V. K. Peterson, N. Sharma, J. Kimpton, B. Johannessen, H. K. Liu, S. X. Dou and Z. Guo, *Chem. Mater.*, 2015, **27**, 3150–3158.

This journal is © The Royal Society of Chemistry 2016

Energy Environ. Sci., 2016, **9**, 3240–3251 | 3251